

Supplemental Information: Thermal controls on ice stream shear margins

by Pierce Hunter, Colin Meyer, Brent Minchew, Marianne Haseloff, and Alan Rempel

S1. CONSISTENCY CHECK ON ADVECTIVE TRANSPORT ASSUMPTIONS

Haseloff and others (2019) present an approximation for in-plane lateral and vertical advection from a supplying ice ridge on a two-dimensional cross-section of variable thickness. An example advection profile using this approximation applied to an ice stream of uniform thickness H is shown in fig. S1. This approach approximates these smaller velocity components effectively, thereby significantly simplifying numerical computations. The analytical solution relies on the depth-averaged mass balance, assuming incompressibility, with uniform ice thickness H , so that

$$\frac{\partial u}{\partial x} + \frac{\partial \bar{v}}{\partial y} = \frac{\dot{a}}{H}, \quad (\text{S1})$$

which requires downstream velocity u . However, since downstream velocity is not known a priori, while the lateral and vertical advective transport approximations we seek are expected to be relatively insensitive to minor errors in the u profile, we approximate this velocity component as negligible within the ridge and use the free-slip solution within the stream, which assumes homogeneous ice rheology, (e.g. Raymond, 2000)

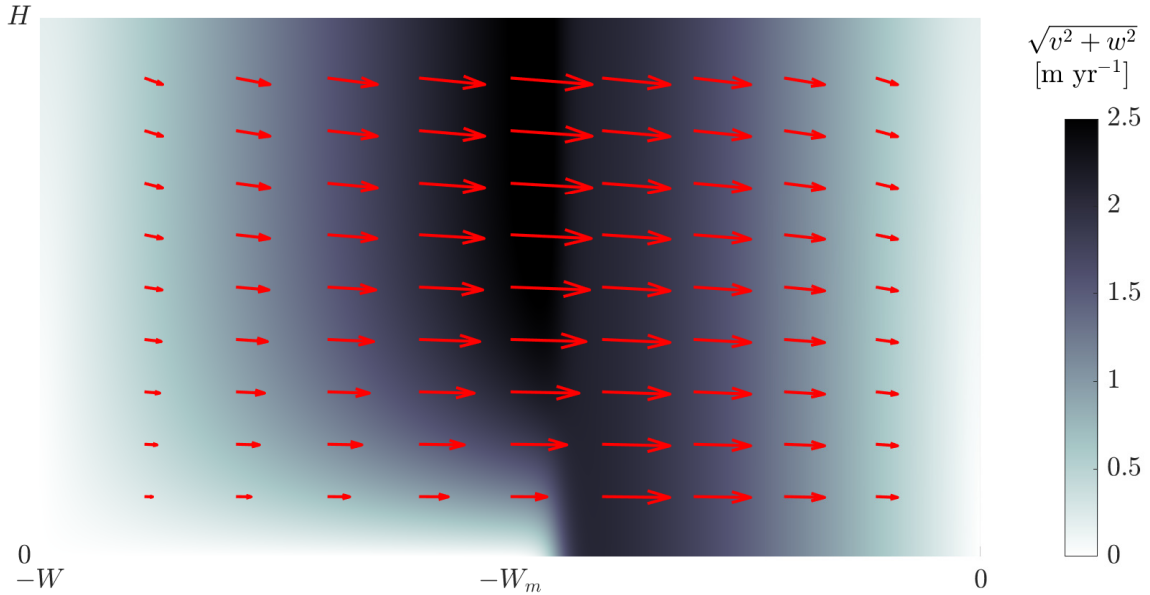


Fig. S1. The combined lateral and vertical advection profile for an idealized stream assuming spatially uniform 20 cm yr^{-1} accumulation and $\delta_y = 2$. We specify no slip under the ridge ($-W \leq -y \leq -W_m$), and fixed basal friction under the stream ($-W_m \leq -y \leq 0$). Lateral velocity v is much greater than vertical velocity w through the majority of the cross-section.

$$u \approx \begin{cases} u_c \left[1 - \left(\frac{y}{W_m} \right)^{n+1} \right] & \text{for } |y| \leq W_m, \\ 0 & \text{for } W_m \leq |y| \leq W. \end{cases} \quad (\text{S2})$$

Figure S2 shows that the approximation for u used in the derivation of v and w is in good agreement with calculated values of downstream velocity for present-day conditions at the three Bindschadler Ice Stream cross-sections examined in the main paper. The approximation differs from the modeled velocity output most significantly near the margin, and most drastically when temperate ice is present (i.e. Downstream-S). The maximum error is between 5 and 10% of the stream center maximum u_c , which is around 400 m yr^{-1} for Upstream-N and Upstream-S, and closer to 700 m yr^{-1} for Downstream-S. The tendency, in the presence of temperate ice, for flow near the margin to be underestimated by a plug flow approximation is consistent with the expectation that temperate ice leads to significant softening within the margin, thus allowing much higher strain rates, and much higher velocities on the stream side of the domain, near the margin. Because lateral advection is driven by flow from the ridge (where our approximation holds more clearly), we do not expect this slight under-estimation in stream velocity near the margin to cause any significant change to our modeled temperature profiles.

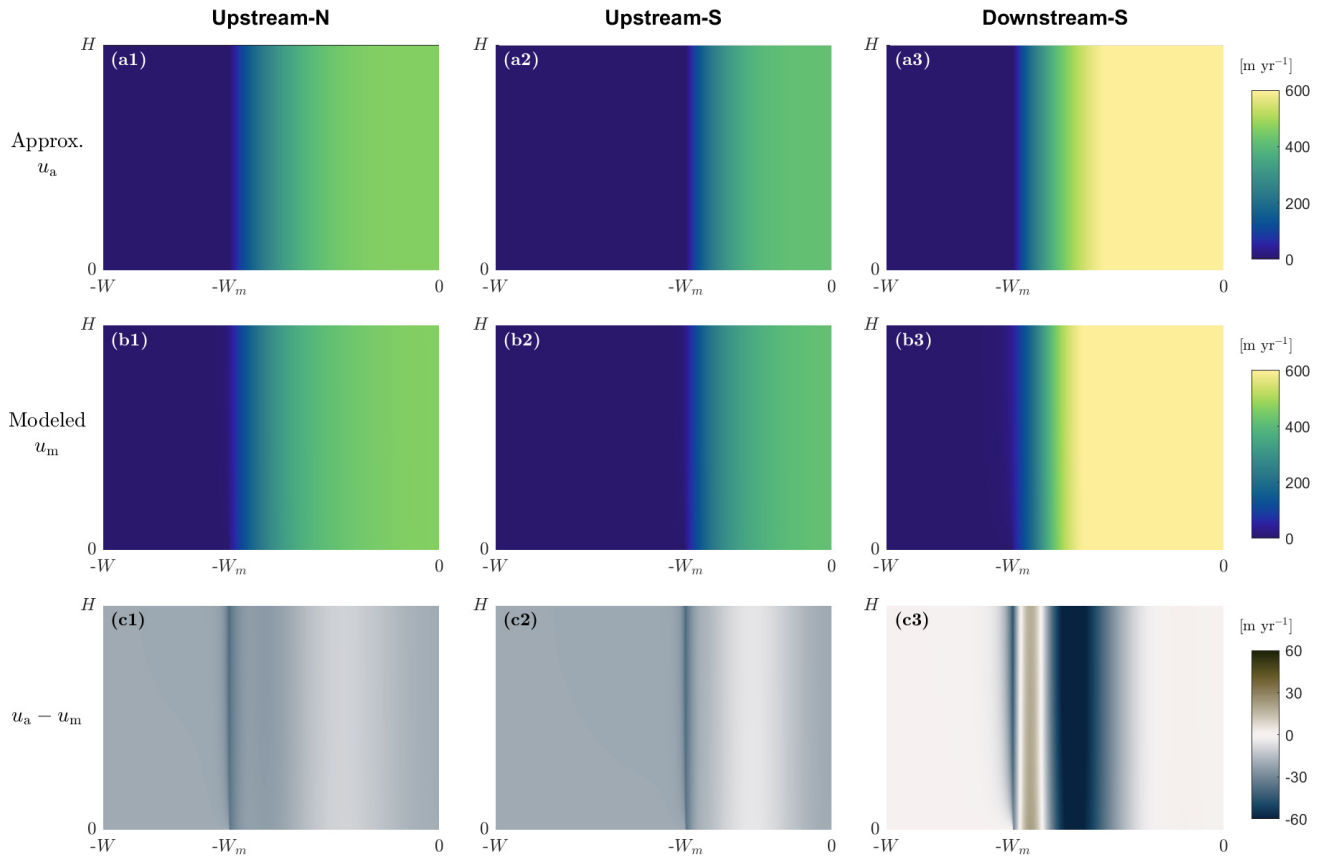


Fig. S2. Here, we show—for each of three BIS cross sections: Upstream-N (column 1), Upstream-S (column 2), Downstream-S (column 3) (see fig. 6 for locations)—(a) approximate velocity profiles using equation (S2) under present day conditions, (b) velocity profiles taken from simulation output, and (c) the difference between the approximate and modeled velocities. The maximum error within each profile is between 5 and 10% of the stream center maximum velocity u_c .

S2. SCALING ANALYSIS

Shear heating vs. advection

We want to analyze the behaviors between the nondimensional parameters found in fig. 5 of the main text, which estimate the requirements for the development of temperate ice, corresponding to a fundamental change in shear margin behavior from cold and rigid, to warm and soft. We look, first, to the energy balance equation where conduction is balanced by advective heat transport and shear heating,

$$\frac{\partial}{\partial y} \left(k \frac{\partial T}{\partial y} \right) + \frac{\partial}{\partial z} \left(k \frac{\partial T}{\partial z} \right) = \rho c \left(v \frac{\partial T}{\partial y} + w \frac{\partial T}{\partial z} \right) - \psi, \quad (\text{S3})$$

which we will use to estimate the behavioral trends between shear heating and advection. This relationship, as seen in fig. 5 of the main text, is not dependent on driving stress. This point is evidenced by taking the plots from fig. 3 of the main text, and overlaying them on top of one another. We stack the plots with the lowest accommodated driving stress (leftmost) on top, and plot contour lines corresponding the same temperate fraction in each panel. The results of this analysis are found in fig. S3, with (a) $\delta_y = 2$ corresponding to the top row of fig. 3, and (b) $\delta_y = 3$ corresponding to the bottom row of fig. 3.

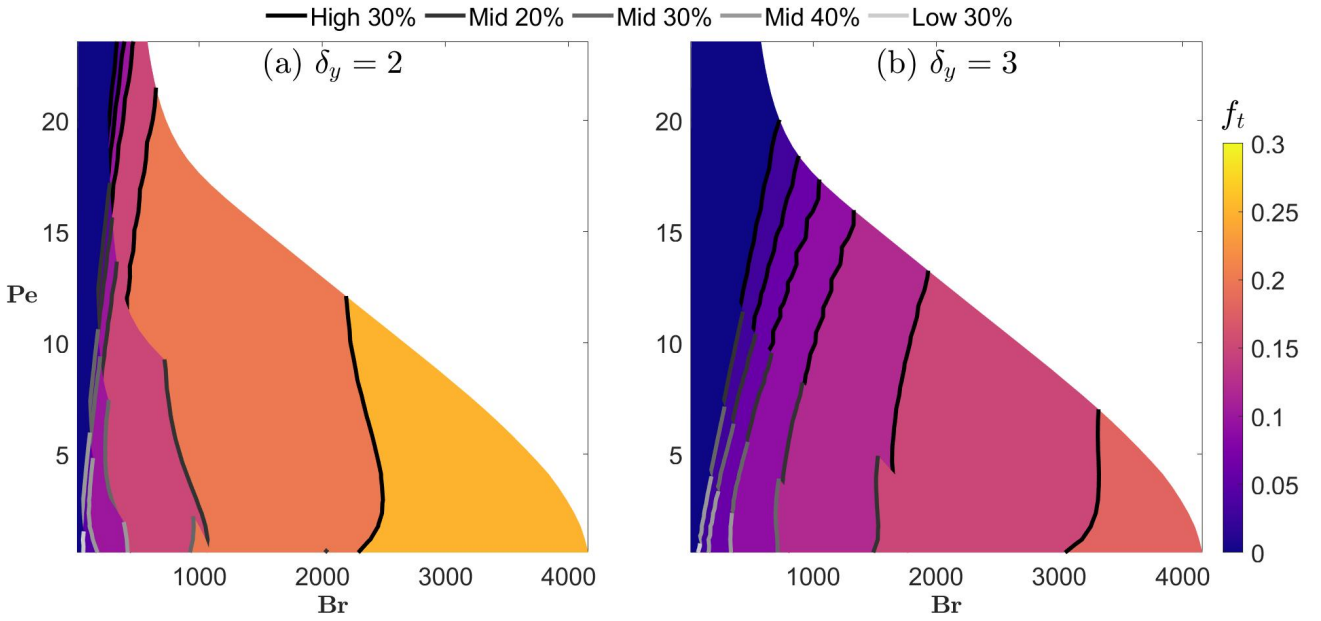


Fig. S3. The plots from fig. 3 overlaid on top of each other with (a) $\delta_y = 2$ and (b) $\delta_y = 3$, plotted in Br–Pe space (see table 2 for definitions). Each panel from fig. 3 is represented by a unique contour line shade. We find that each contour line is nearly continuous, an indicator that—for each set of geometric bounds—temperate volume is almost entirely controlled by Pe and Br and much less sensitive to driving stress.

Figure 5 in the main paper demonstrates clear and consistent scaling relationships for \mathbf{Ga}_{\max} and the corresponding value of Br. To build further understanding of these relationships, we are drawn to examine how the energy balance scales near the melting point. Accordingly, we define a scale for each variable as:

$$[k] = k_0, \quad (\text{S4})$$

$$[c] = c_0, \quad (\text{S5})$$

$$[v] = \frac{\dot{a}}{H} (W - W_m), \quad (\text{S6})$$

$$[w] = \dot{a}, \quad (\text{S7})$$

$$[T] = T_m - T_s = \Delta T, \quad (\text{S8})$$

$$[y] = W_m, \quad (\text{S9})$$

$$[z] = H, \quad (\text{S10})$$

$$[\psi] = A_0^{-1/n} \left(\frac{u c}{L} \right)^{(n+1)/n}. \quad (\text{S11})$$

Here, $k_0 = k(0^\circ\text{C})$, $c_0 = c(0^\circ\text{C})$, $A_0 = A(0^\circ\text{C})$, W is the domain half-width, W_m is the ice stream half-width, H is the ice thickness, \dot{a} is the average annual accumulation rate, u_c is the stream center velocity, and L is a representative length scale.

We can now approximate the energy balance in equation (S3) using these scales while isolating shear heating, which yields

$$A_0^{-1/n} \left(\frac{u_c}{L} \right)^{(n+1)/n} = \frac{\rho c_0 \dot{a} \Delta T}{H} \delta_y - \frac{k_0 \Delta T}{W_m^2} - \frac{k_0 \Delta T}{H^2}, \quad (\text{S12})$$

where $\delta_y \equiv W/W_m$. Dividing all terms by the vertical conduction and defining another aspect ratio $\delta_z \equiv H/W_m$ gives the relation

$$\frac{A_0^{-1/n} u_c^{(n+1)/n} H^{(n-1)/n}}{k_0 \Delta T} \left(\frac{H}{L} \right)^{(n+1)/n} = \frac{\rho c_0 \dot{a} H}{k_0} \delta_y - \delta_z^2 - 1. \quad (\text{S13})$$

Plugging in **Br** and **Pe** where applicable (see table 2 in the main text) simplifies the expression to

$$\left(\frac{A_*}{A_0} \right)^{1/n} \text{Br} \left(\frac{H}{L} \right)^{(n+1)/n} = \text{Pe} \delta_y - \delta_z^2 - 1; \quad (\text{S14})$$

and solving for **Br**, while recognizing that shear margin dimensions are comparable to ice depth so that $L \sim H$, gives the relationship

$$\text{Br} = \left(\frac{A_0}{A_*} \right)^{1/n} \left[\text{Pe} \delta_y - \delta_z^2 - 1 \right]. \quad (\text{S15})$$

We prefer to give relations to δ_y in terms of the ridge extent $(\delta_y - 1)$, so the final form of the energy balance that emerges from our scaling analysis becomes (using $\bar{A} \equiv A_0/A_*$)

$$\text{Br} = \bar{A}^{1/n} \text{Pe} (\delta_y - 1) + \bar{A}^{1/n} \text{Pe} - \bar{A}^{1/n} (\delta_z^2 + 1). \quad (\text{S16})$$

In fig. 5 of the main text we see the relation between **Br** and **Pe** (while holding δ_y constant), such that

$$\text{Br} = 2.60 \text{Pe} + 0.36; \quad (\text{S17})$$

and using the scaling analysis presented here we would expect the relationship

$$\text{Br} = 3.8 \text{Pe} - 1.9. \quad (\text{S18})$$

The scaling analysis matches the linear dependence and has coefficients with the correct magnitudes, though they do differ from those produced by the numerical model; the offset may partly be ascribed to the thermoviscous feedback that is not fully captured by the Brinkman number (which does not include the temperature dependence of viscosity). We also compare the model results with the predicted relation between **Br** and $(\delta_y - 1)$. Our model predicted the linear relation

$$\text{Br} = 15.00 (\delta_y - 1) + 0.59, \quad (\text{S19})$$

and the scaling analysis done here predicts the relation

$$\text{Br} = 11.2 (\delta_y - 1) + 9.27. \quad (\text{S20})$$

Again, the scaling analysis performed here predicts the linear relationship between shear heating and the ridge extent, while the coefficients differ somewhat.

Gravitational forcing vs. thickness-to-width ratio

We now turn to the thickness-to-width ratio (δ_z) and explore what control that has on the system, starting with the global ice stream force equilibrium, expressed as

$$\rho g H \sin \alpha W_m = \tau_b W_m + \eta \frac{\partial u}{\partial y} H, \quad (\text{S21})$$

so that the net downstream driving force of gravity is balanced by basal friction and viscous lateral drag. A key feature of this system is the large changes in viscosity with temperature over the model domain. To evaluate the scale of viscous stresses, we focus on the near-margin region, where velocity changes dramatically over a horizontal length scale L (i.e. $[\partial u / \partial y] \sim u_c / L$) and we approximate the characteristic viscosity as

$$[\eta] = A_0^{-1/n} \left(\frac{u_c}{L} \right)^{(1-n)/n}. \quad (\text{S22})$$

Expressing τ_b as a fraction f_{τ_b} of the driving stress ($f_{\tau_b} \rho g H \sin \alpha$), and rearranging equation (S21) yields

$$(1 - f_{\tau_b}) \frac{A_0^{1/n} \rho g H L^{1/n} \sin \alpha}{u_c^{1/n}} = \delta_z, \quad (\text{S23})$$

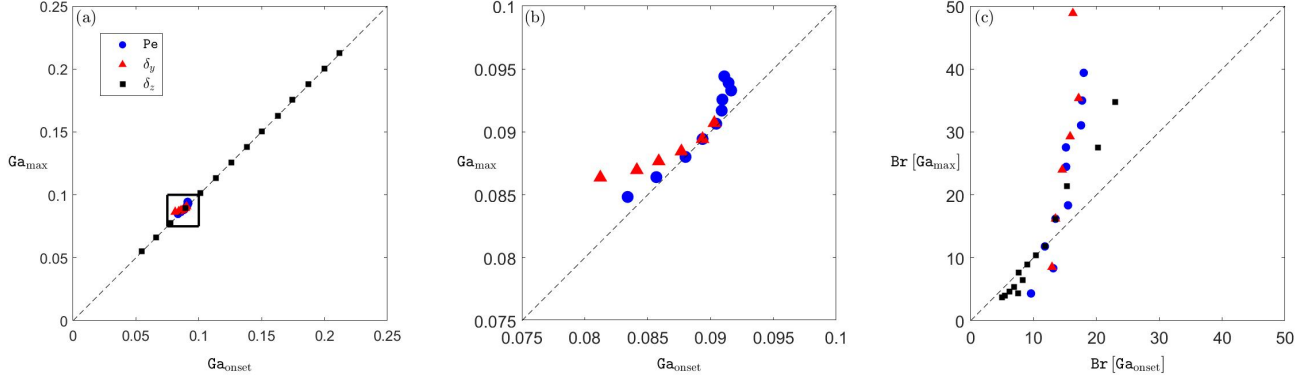


Fig. S4. (a) Ga_{onset} plotted against Ga_{max} for each of the scenarios detailed in fig. 4 of the main text. (b) the same data zoomed in on the region depicted by the black square, with the δ_z data excluded. (c) $\text{Br}[\text{Ga}_{\text{onset}}]$ plotted against $\text{Br}[\text{Ga}_{\text{max}}]$ for each of the three scenarios. The 1:1 line for each plot is traced by the black dashed line.

so that upon substituting in for Ga (see table 2 in the main text) we obtain

$$(1 - f_{\tau_b}) \left(\frac{A_0 L}{A_* H} \right)^{1/n} \text{Ga} = \delta_z. \quad (\text{S24})$$

Solving for Ga , while approximating the margin length scale as comparable to the ice depth so that $L \sim H$ and defining the relation $\bar{f}_{\tau_b} \equiv (1 - f_{\tau_b})$, gives the final form

$$\text{Ga} = \bar{A}^{-1/n} \bar{f}_{\tau_b}^{-1} \delta_z. \quad (\text{S25})$$

The relation we find in fig. 5 of the main text is

$$\text{Ga} = 1.20 \delta_z - 0.032, \quad (\text{S26})$$

and using equation (S25) we get the relationship

$$\text{Ga} = 0.75 \delta_z, \quad (\text{S27})$$

so, much like in the advection vs. shear heating case, we are able to capture the overall behavioral trends inherent in the system, but are unable to match the subtlety of the thermoviscous feedback.

Galilei number: Temperate onset vs. maximum value

In our idealized ice stream study, we present the best fit lines for the location of the maximum Galilei value under a series of targeted parameter sweeps. Here we compare Ga_{max} to the value for temperate onset Ga_{onset} , denoted by filled markers in fig. 4 from the main text. We note that in the colder regimes (i.e. high Pe , high δ_y , or low δ_z) Ga_{onset} occurs before Ga_{max} is reached, with the opposite true for warmer regimes. This behavior suggests, in the case of a colder margin, a larger temperate zone is required to initiate the shift in shear margin behavior from cold and rigid, to warm and soft; in the case of a warmer regime this shift in behavior may occur before any temperate ice is present in the system. Figure S4 shows the linear relation between Ga_{onset} and Ga_{max} when δ_z is varied; in this scenario $\text{Ga}_{\text{onset}} \approx \text{Ga}_{\text{max}}$ leading to the near perfect linearity. Plot (b) zooms in on the boxed region within plot (a), and isolates the cases where advection rates are varied (i.e. Pe or δ_y). While the relation here is still semi-linear in nature, Ga_{max} does increase at a slightly higher rate as Ga_{onset} increases. We also do a similar comparison for the corresponding Brinkman values ($\text{Br}[\text{Ga}_{\text{onset}}]$ vs $\text{Br}[\text{Ga}_{\text{max}}]$), which is presented in plot (c), and find that the amount of shear heating required to reach Ga_{max} increases drastically in the colder regimes, whereas the shear heating to initiate temperate onset does not change as dramatically.

S3. RESOLUTION ANALYSIS

To examine the accuracy of our numerical approach we focus on the slip/no-slip transition point along the bed, which is the only discontinuity in our model domain. We want to ensure that the discontinuity is resolved well enough for the primary model outputs (T , u) to converge, but that the mesh is not so dense as to be computationally infeasible. To test accuracy we looked at a series of built-in and custom resolutions. To illustrate this we pick three different resolutions in nondimensional space, a low resolution (minimum element size 2×10^{-5} , maximum size 6.4×10^{-3}), a high resolution (5×10^{-6} minimum, 1.6×10^{-3} maximum), and a variable resolution (1×10^{-5} minimum, 1×10^{-2} maximum). For the low and high resolution cases we allow COMSOL to choose the resolution throughout the domain, and in the variable case we force higher resolution near

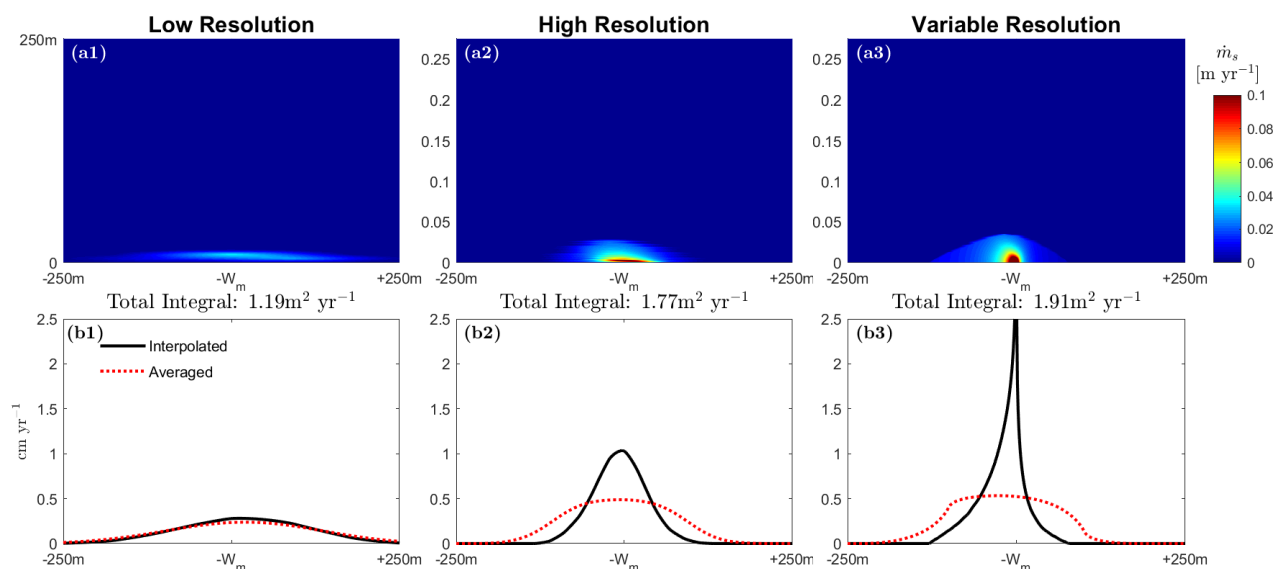


Fig. S5. Shear melt rates from the Upstream-S cross section of Bindschadler under emissions scenario RCP 8.5 conditions predicted at the year 2300. The top image is zoomed into the slip/no-slip transition with 250 m on either side of the singularity, and a vertical extent of 250 m shown. We would not expect to see temperate ice in this region under these conditions, however, when the data is interpolated we do see shear melting. When vertically integrated these interpolated values give non-negligible shear melt rates. To remedy this we instead use a moving average over 200 m increments for shear melt rate only (as opposed to melting from friction along the bed). We also give the shear melt rate, integrated laterally across this 500 m region, suggesting that even with high resolution, the singularity is integrable and provides a relatively small amount of meltwater to the subglacial system.

the discontinuity. For each resolution, we run a simulation on a model geometry from our BIS case study (Upstream-S) under RCP 8.5 conditions predicted at year 2300. This simulation is useful for a resolution analysis because, although this simulation produces temperate ice, we do not expect it to be concentrated at the slip/no-slip boundary. However, due to temperate ice forming elsewhere in the domain, the strain rates under these conditions are high enough to give the appearance of temperate ice having been produced at the transition point.

To get the shear melt-rate profile for each simulation we extract the data from the model, which is given as three column vectors—one for y , one for z , and the last for the shear melt rate \dot{m}_s —and cast this to a regular grid, which can then be integrated vertically for basal melt distribution, and both laterally and vertically for total meltwater supply. We utilize interpolation techniques to get values within the domain, but this only works for grid points sufficiently far from the stress singularity. As seen in fig. S5, where the top row is a natural interpolation (continuous under differentiation), the high strain rates from the singularity produce a small, non-negligible temperate ice zone. When the values are integrated vertically to get a melt distribution rate at the bed (shown in fig. S5, bottom row, solid black line) we see melt rates upwards of 2 cm yr^{-1} , which is comparable to the total melt distribution rates given in fig. 8. These values result from high strain-rates near an integrable singularity that is characterized by a finite total rate of heat input. To reduce model sensitivity to grid resolution near the singularity, we calculate moving averages over a fixed 200 m horizontal dimension, providing more representative melt rates shown with the red lines in the bottom row of fig. S5. As expected, we find that the rate of melt input at the slip/no-slip boundary is relatively small, and the total melt production near the singularity is nearly independent of the grid resolution. When the same averaging procedure is followed away from the slip/no-slip transition, the results match the interpolated values.

REFERENCES

- Haseloff M, Hewitt IJ and Katz RF (2019) Englacial pore water localizes shear in temperate ice stream margins. *Journal of Geophysical Research: Earth Surface*, **124**(11), 2521–2541, ISSN 21699011 (doi: 10.1029/2019JF005399)
- Raymond CF (2000) Energy balance of ice streams. *Journal of Glaciology*, **46**(155), 665–674, ISSN 00221430 (doi: 10.3189/172756500781832701)